

2 Planar Pixel Sensors for the ATLAS Upgrade: Beam 3 Tests results

J. Weingarten^{1*}, S. Altenheiner², M. Beimforde³, M. Benoit⁴, M. Bomben⁵, G. Calderini^{5,6}, C. Gallrapp⁴, M. George¹, S. Gibson⁴, S. Grinstein⁷, Z. Janoska⁸, J. Jentsch⁴, O. Jinnouchi⁹, T. Kishida⁹, A. La Rosa¹⁰, V. Libov¹¹, A. Macchiolo³, G. Marchiori⁵, D. Münstermann⁴, R. Nagai⁹, G. Piacquadio⁴, B. Ristic², I. Rubinskiy¹¹, A. Rummler², Y. Takubo¹², G. Troska², S. Tsiskaridze⁷, I. Tsurin¹³, Y. Unno¹², P. Weigell³, T. Wittig²

¹*II. Physikalisches Institut, Georg-August-Universität Göttingen, Germany*

Email: jens.weingarten@uni-goettingen.de

²*Technische Universität Dortmund, Fakultät Physik, Dortmund, Germany*

³*Max-Planck-Institut für Physik, München, Germany*

⁴*CERN, Genève, Switzerland*

⁵*Laboratoire de Physique Nucleaire et de Hautes Énergies (LPNHE), Paris, France*

⁶*Dipartimento di Fisica E. Fermi, Università di Pisa, and INFN Sez. di Pisa, Pisa, Italy*

⁷*Institut de Física d'Altes Energies (IFAE), Bellaterra, Spain*

⁸*Division of elementary particle physics - Institute of Physics of the Academy of Sciences of the Czech Republic, Prague, Czech Republic*

⁹*Tokyo Institute Of Technology, Tokyo, Japan*

¹⁰*Section de Physique (DPNC), Université de Genève, Genève, Switzerland*

¹¹*Deutsches Elektronen-Synchrotron (DESY), Hamburg, Germany*

¹²*High Energy Accelerator Research Organization, Tsukuba, Japan*

¹³*The University of Liverpool, Liverpool, United Kingdom*

4

ABSTRACT: The performance of planar silicon pixel sensors, in development for the ATLAS Insertable B-Layer and High Luminosity LHC (HL-LHC) upgrades, has been examined in a series of beam tests at the CERN SPS and DESY facilities since 2009. Salient results are reported on the key parameters, including the spatial resolution, the charge collection efficiency and the charge sharing between adjacent cells, for different bulk materials.

5 Measurements are presented for n⁺-in-n pixel sensors irradiated with a range of fluences and for p-type silicon sensors with slightly differing layouts from several vendors. All tested sensors were connected via bump-bonding to the ATLAS Pixel read-out chip.

The tests reveal that both n-type and p-type planar sensors are able to collect significant charge even after the lifetime fluence expected at the HL-LHC.

6 KEYWORDS: Silicon pixel detectors, planar sensors, radiation damage to detector materials (solid
7 state), beam tests, simulations, ATLAS upgrade, HL-LHC, SLHC.

9 Contents

10	1. Introduction	1
11	2. Beam test setup	2
12	2.1 The EUDET telescope	2
13	2.2 Devices Under Test	3
14	3. The beam test analysis	4
15	3.1 Track reconstruction	4
16	3.2 Detector alignment	4
17	3.3 Data analysis	5
18	4. The n-in-p demonstrator program	5
19	4.1 CiS sensors	6
20	4.1.1 Sensor design	6
21	4.1.2 Beam test results	7
22	4.2 HPK sensors	12
23	4.2.1 Sensors design	12
24	4.2.2 Beam test results	12
25	5. Radiation hardness of n-in-n sensors	14
26	5.1 Results	16
27	6. Slim Edge	20
28	7. Conclusion	22

30 1. Introduction

31 The ATLAS collaboration will upgrade the current Pixel Detector [1] in two phases. A first upgrade
 32 will be realized during the shut-down in 2013, by inserting a fourth detection layer (Insertable B-
 33 Layer - IBL) at a radius of 3.2 cm from the beam line. The IBL will improve the tracking and
 34 vertexing performance of the current pixel detector significantly during operation of the LHC at its
 35 nominal centre-of-mass energy ($\sqrt{s} = 14$ TeV) [2].

36 The close proximity to the interaction point imposes a very harsh radiation environment on the
 37 IBL. At the end of Phase-I operation of the LHC, foreseen around 2020, the IBL must sustain an
 38 estimated fluence of 5×10^{15} n_{eq}/cm², including a 60% safety factor at $r = 3.2$ cm.

*Corresponding author.

39 The Phase-II luminosity upgrade for the LHC (beyond 2020) aims to increase the instanta-
40 neous luminosity to $5 \times 10^{34} \text{ cm}^{-2} \text{ s}^{-1}$, posing a serious challenge to the technology for the AT-
41 LAS tracker in the High Luminosity era (HL-LHC): the lifetime fluence for the innermost layer,
42 including safety factors, is estimated to be on the order of $2 \times 10^{16} \text{ n}_{\text{eq}}/\text{cm}^2$ [3]. Hence, in view of
43 a possible pixel system replacement after 2020, new pixel sensors are under study.

44 Within the Planar Pixel Sensor collaboration (PPS) [7] several optimizations of this well-
45 known technology are under investigation, to address issues arising from the LHC upgrades. The
46 PPS collaboration investigates the suitability of different materials (p- and n-bulk, diffusion oxy-
47 genated float zone, magnetic Czochralski) and different geometries (slim edge design, number and
48 width of guard rings) for a new generation of planar pixel sensors. Data taken during beam tests
49 complement tests under laboratory conditions in assessing the performance of various sensor pro-
50 totypes. In this paper results from two beam test campaigns in 2010 are presented.

51 The paper is organized as follows. After a description of the experimental setup of the beam
52 tests in Section 2 and some details of the data analysis in Section 3, beam test results are presented
53 on three areas of the scientific program of the PPS collaboration:

54 Sensors implemented in p-type silicon are being studied by several groups within the PPS
55 collaboration. Section 4 shows results from the first beam test operation of various prototype
56 sensors. We will show that the performance of p-type sensors in terms of collected charge, charge
57 sharing probability, and spatial resolution is very similar to that of n-type sensors.

58 In Section 5 the radiation-hardness of sensors implemented in n-type diffusion oxygenated
59 float-zone silicon are studied. We will show that n-in-n detectors are operable at the nominal bias
60 voltage of 1000 V after a fluence comparable with that expected for IBL ($5 \times 10^{15} \text{ n}_{\text{eq}}/\text{cm}^2$). Noise
61 occupancy, charge collection performance, charge sharing probability and spatial resolution will be
62 presented.

63 The new pixel sensors will not only have to sustain the harsher environment, but also have to
64 show high geometrical acceptance without overlapping adjacent modules. Hence the inactive areas
65 of the future pixel sensor have to be reduced significantly. For this reason, efforts were devoted
66 to design detectors with reduced dead area. The “slim edge” detector-concept will be presented in
67 Section 6, together with its performance in terms of charge collection at the detectors’ edge.

68 **2. Beam test setup**

69 Beam tests are crucial for characterizing the performance of any particle detector. Planar silicon
70 sensors for the ATLAS upgrade have been evaluated in several beam tests in 2009 and 2010. Data
71 presented in this paper were taken in two different periods in 2010 at the CERN SPS beamline H6.
72 In both periods pion beams of 120 GeV/c were used. The high momentum of the beam particles
73 minimizes the influence of multiple scattering, enabling high precision tracking using the EUDET
74 beam telescope [8].

75 **2.1 The EUDET telescope**

76 The telescope consists of six equal planes, divided into two groups (arms) of three planes each.
77 The Devices Under Test (DUTs) are mounted in between these two arms of the telescope as well as
78 downstream of the last telescope plane. The increase of the track extrapolation error downstream

79 of the telescope was minimized by mounting the DUTs as close as possible to the last telescope
80 plane.

81 The sensitive elements of the telescope planes are Mimosas26 [25] active pixel sensors with a
82 pixel pitch of $18.4\ \mu\text{m}$. Each plane consists of 1152×576 pixels covering an active area of
83 $21.2 \times 10.6\ \text{mm}^2$. The tracking resolution between the telescope arms is estimated to be $2\ \mu\text{m}$,
84 at the position of the samples downstream of the telescope it is approximately $10\ \mu\text{m}$. [26]

85 A coincidence of four scintillators (two upstream and two downstream of the telescope) was used
86 for triggering, which resulted in an effective sensitive area of $2 \times 1\ \text{cm}^2$.

87 2.2 Devices Under Test

88 All DUTs were read out using the current ATLAS Pixel readout chip (FE-I3) [9]. The FE-I3 chip
89 is an array of 160 rows \times 18 columns of $50\ \mu\text{m} \times 400\ \mu\text{m}$ read-out cells. In each readout cell the
90 sensor charge signal is amplified and compared to a programmable threshold by a discriminator.
91 The information on the collected signal is encoded through a digital time over threshold (ToT) [9]
92 measured in units of 25 ns, which is the nominal LHC bunch crossing rate. The ToT to charge
93 conversion was tuned for each individual pixel to 60 ToT for a deposited charge of 20 ke. Discrim-
94 inator thresholds were tuned to a charge of 3.2 ke. Prior to the beam test, tuning was performed
95 for every readout chip in realistic conditions, designed to closely resemble those at the beam test.
96 Since the ToT-tuning is particularly temperature dependent, the ToT was calibrated on each sample
97 after installation in the beam test setup to ensure a proper charge conversion.

98 For each DUT a fiducial region was defined, based on geometrical and operability consider-
99 ations. For most studies only the performance of central pixels is of interest. Therefore in many
100 analyses the pixels at the edges of the sensors were masked. In addition, all pixels that were found
101 to have disconnected or merged bump-bonds in laboratory measurements were masked, as were
102 pixels with high noise occupancy.

103 Devices were irradiated to different fluences using 25 MeV energy protons at the Irradiation
104 Center in Karlsruhe [19], 24 GeV/c momentum protons at the CERN PS irradiation facility [12]¹,
105 and reactor neutrons at the TRIGA reactor of the Jožef Stefan Institute, Ljubljana [18]. The radi-
106 ation damage from the different irradiations is scaled to the equivalent damage from 1 MeV neu-
107 trons using the NIEL hypothesis [30]. During the irradiations the devices were neither powered
108 nor cooled. No standardized annealing procedure was used, but samples were stored below $0\ ^\circ\text{C}$
109 to avoid uncontrolled annealing. The FE-I3 was designed for a lifetime irradiation dose of 1 kGy.
110 Some of the DUTs were irradiated to significantly higher doses, leading to increasing numbers of
111 non-working pixels.

112 For the beam tests, irradiated DUTs were cooled via a strip of copper tape thermally connecting
113 the backside of the DUTs with the base plate of the thermal enclosure. The base plate was in turn
114 cooled using dry ice (CO_2) [17]. Due to this setup, the temperature of the sensors varied over time
115 as the dry ice evaporated and needed to be closely monitored. Temperatures were recorded, ranging
116 between $-45\ ^\circ\text{C}$ shortly after filling the coldbox with dry ice and $-15\ ^\circ\text{C}$ towards the end of a data
117 taking period.

¹we observed FE-I3 chip stopped working after being CERN PS irradiated

118 **3. The beam test analysis**

119 **3.1 Track reconstruction**

120 The tracks of particles traversing the EUDET telescope are reconstructed from raw hit positions
121 by a sequential algorithm. In the first step, the hits recorded in all telescope planes and DUTs
122 are converted into the EUTelescope [23] internal data format. A time stamp issued by the Trigger
123 Logic Unit (TLU) [24] is attached to each hit, enabling recovery from any loss of synchronisation
124 between telescope and DUTs during this step, provided the desynchronisation is not too severe.

125 As the Mimosas26 sensors of the telescope plane use the rolling shutter read-out technique, the
126 telescope integrates hits for $112\ \mu\text{s}$ after the arrival of the trigger signal. This is much longer than
127 the $400\ \text{ns}$ hit-buffer of the DUTs, so some tracks will be recorded by the telescope, but not by the
128 DUTs. To correct for this effect, only hits that were recorded within the sensitive time of the DUTs
129 are retained for further analysis. This is done by requesting hits spatially associated to the track in
130 one or more of the other DUTs (in-time tracks). A clustering algorithm is then executed searching
131 for clusters in all planes.

132 Hits are then transformed from the local coordinate system of each plane to a global coordinate
133 system, where the z -axis gives the beam direction. During this coordinate transformation the pixel
134 sizes in x - and y -directions, the specified z -position of all sensors, and the rotations of the DUTs
135 about all axes are taken into account. Based on correlations between hit positions in different planes
136 in the global frame, a coarse pre-alignment is calculated. Using this information, the alignment
137 processor (see also 3.2) tries to fit tracks through all planes in the setup, taking into account the
138 different spatial resolutions of the planes and individual track selection criteria for each plane.
139 Individual selection criteria are especially necessary, since the pixel size of the telescope-planes
140 is $18.4\ \mu\text{m}$ in both directions, whereas the investigated FE-I3 based samples have a pixel size of
141 $400\ \mu\text{m} \times 50\ \mu\text{m}$.

142 The final step is the track-fitting, which is based on a Kalman filter [29]. The track fits are
143 unbiased, requiring a hit in at least four out of the six telescope planes and in at least one DUT. Also
144 in this step, different track selection criteria can be applied. The parameters of all reconstructed
145 tracks are finally stored in a ROOT file [31] for further analysis (see Section 3.3).

146 **3.2 Detector alignment**

147 The alignment for the telescope planes and the DUTs in the EUTelescope track-reconstruction uses
148 the MILLIPEDE tool [27]. In the algorithm the alignment constants are calculated such that the
149 uncertainties of the fitted track parameters, as well as the χ^2 of the track residuals, are minimized.
150 Straight line fits to the hit positions in all active planes are performed independently for the x - and y -
151 directions. Individual criteria can be applied to the resulting residual distributions to suppress fake
152 tracks. In the alignment process the pre-alignment constants, calculated in the previous hitmaker
153 step, are taken into account. This enables alignment of all telescope-planes and DUTs in one step,
154 where just the first telescope-plane is fixed in its position and orientation. The alignment constants
155 are applied in the final track fitting process.

156 3.3 Data analysis

157 The analysis of the reconstructed tracks is conducted in several steps, using a dedicated data anal-
158 ysis framework (tbmon) [28].

159 Firstly, unresponsive and noisy pixels are identified and masked. A pixel is unresponsive if
160 it registers no hit during the full data taking period and noisy if more than 5×10^{-4} of all hits
161 registered in this pixel are not correlated with a beam particle. Typically, less than 1 % of pixels are
162 masked in non-irradiated modules; for irradiated devices the fraction fluctuates between samples.
163 On average, roughly 10 % of the pixels have to be masked due to problems with settings of the
164 readout chip or increased noise due to high leakage current of the sensor.

165 In the following analyses tracks extrapolated from the telescope are “matched” to a hit if the hit
166 and the extrapolated track impact point in the DUT plane containing the hit are closer than $400 \mu\text{m}$
167 in the long pixel direction and $150 \mu\text{m}$ in the short pixel direction. The hit position is defined as
168 the η corrected ToT weighted position of all pixels in a cluster [13].

169 To estimate the intrinsic spatial resolution of the DUTs the distribution of hit residuals is
170 studied. The hit residual is defined as the distance between the reconstructed hit position on the
171 DUT and the extrapolation of the fitted track to the DUT plane. The intrinsic spatial resolution
172 is estimated by the RMS of the residual distribution for clusters of all sizes, while the residual
173 distribution of 2-pixel clusters is used to estimate the width of the area between pixels, where
174 charge sharing occurs. The distribution is fitted with the sum of two Gaussian functions, where one
175 accounts for mis-reconstructed hits, resulting in large residual values (equal to 2 times the pixel
176 pitch or more), and the other for correctly reconstructed hits. The width of this “core” Gaussian
177 gives the width of the charge sharing region.

178 To calculate the charge sharing probability for each hit within a cluster, it is determined
179 whether a hit is found in a pixel cell adjacent to the one matched to a track. This probability
180 increases towards the edge of the pixel since charge carriers are more likely to drift to the neigh-
181 bouring pixel. The corresponding plot, referred to as a charge sharing map, is centred on one pixel,
182 also showing half of the adjacent pixel in each direction. The overall charge sharing is defined
183 as the number of tracks with at least one hit in a neighbouring pixel divided by the number of all
184 tracks.

185 Due to a problem in the readout system, random DUTs stopped sending data for random short
186 intervals. Therefore, the availability of a reference plane for the selection of in-time tracks cannot
187 be ensured at all times. As this selection is crucial for the measurement of the hit efficiency, this
188 analysis could not be done with the available data, while charge collection and spatial resolution
189 measurements are unaffected.

190 4. The n-in-p demonstrator program

191 While n-type bulk sensors require patterned guard rings on the back side of the sensor, for p-type
192 material these can be moved to the pixelated side of the sensor (front side); then metallization is
193 the only process for the back side. This makes it a very cost-effective material for future pixel
194 detectors. On the other hand the high voltage, which is applied to the back side of the sensor, is
195 also present on the edges of the front side of the sensor facing the read-out chip, which is at ground

196 potential. Thus spark discharges may occur, posing a risk to the readout electronics itself. This can
 197 be limited by the deposition of an insulating coating on the edge of the sensor; more details are
 198 given in the next section.

199 Sensors in p-type technology tested in 2010 were produced at CiS² and at HPK³. Table 1 summa-
 200 rizes the relevant quantities for the devices studied in the beam test. Further details of each sample
 201 are described below.

sample	Period	fluence (10^{15} n _{eq} /cm ²)	irradiation type	V_{bias} [V]
MPP1	July	0	–	150, 200
MPP2	July	0	–	150, 200
MPP3	October	0	–	150
MPP4	October	1	reactor neutrons	250, 350, 500, 550, 700
MPP5	October	1	25 MeV protons	500, 550
KEK1	October	0	–	100, 200
KEK2	October	0	–	100, 200

Table 1. Relevant quantities of the n-in-p samples.

202 4.1 CiS sensors

203 In the following the p-type sensors produced at CiS will be introduced and their beam test results
 204 discussed.

205 4.1.1 Sensor design

206 The n-in-p pixel sensors labelled as MPP1–MPP5 were produced at CiS with a geometry compat-
 207 ible with FE-I3, in the framework of a common RD50 production [20]. They were made from
 208 Diffusion Oxygenated Float Zone (DOFZ) 285 μm thick wafer, with 100 crystal orientation and a
 209 wafer resistivity of 15 k Ωcm . The depletion voltage before irradiation was nominally 60 V.

210 Two guard rings structures with differing widths have been implemented and tested. One
 211 design has the standard inactive area of 1 mm per side of normal ATLAS pixel sensors, while the
 212 other has a reduced inactive area, as illustrated in Figure 1. MPP1, MPP3 and MPP5 have 19
 213 guard-rings, with the standard total inactive width of 1 mm on each side. The samples MPP2 and
 214 MPP4 (see Table 1) have 15 guard-rings with a total inactive area of 610 μm on each side. For both
 215 guard rings designs the bias ring and the inner guard ring are wider than the other ones, enabling
 216 tests of the sensors before connection to the read-out chips. The external guard ring widths grows
 217 with promixity to the cutting edge from 17 μm to 22 μm , with the gap between the rings from 5
 218 to 8 μm . The distance between the last ring and the dicing edge is 400 μm for the 19 guard rings
 219 design while it is 100 μm in the 15 guard rings design.

220 The inter-pixel isolation is achieved by means of a homogenous p-spray implantation.

221 A BCB (Benzocyclobutene) coating has been applied to the pixelated side of the n-in-p pixel
 222 sensors, to prevent sparks between the area outside the guard ring area, that is at the same high

²Forschungsinstitut für Mikrosensorik und Photovoltaik GmbH

³Hamamatsu Photonics K. K.

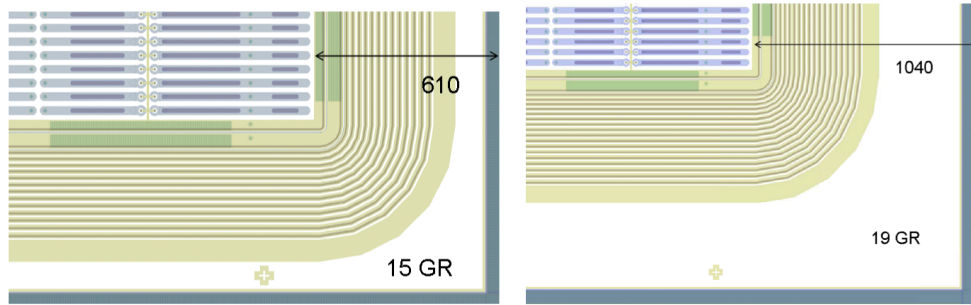


Figure 1. Left: View of a corner of an n-in-p sensor of the CiS production with 15 guard rings. Right: View of a corner of an n-in-p sensor of the CiS production, with 19 guard rings.

223 potential as the back side, and the chip, at ground potential (Figure 2). The interconnection to the
 224 chips has been performed via bump-bonding at IZM-Berlin ⁴.

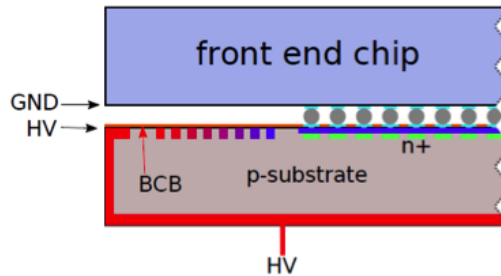


Figure 2. Schematics of a CiS n-in-p pixel assembly. The potential of the different parts is given. The BCB layer is indicated in orange.

225 4.1.2 Beam test results

226 As documented in Table 1, during the first beam test period (July 2010) none of the CiS n-in-
 227 p sensors (namely MPP1, MPP2) were irradiated. In the second period (October 2010) MPP4
 228 was tested after irradiation with reactor neutrons [18] to a fluence of $1 \times 10^{15} \text{ n}_{\text{eq}}/\text{cm}^2$ and MPP5
 229 was irradiated with low energy protons (25 MeV) at the cyclotron of the Karlsruhe Institute of
 230 Technology (KIT) [19] to the same equivalent fluence. MPP3 was kept as an unirradiated reference.
 231 The performance of these five samples is presented as follows.

232 **Cluster size** The cluster size distribution was studied for all sensors as a function of the bias
 233 voltage. A detailed breakdown is reported in Table 2. For the non-irradiated sample roughly 70 %
 234 of the clusters consisted of a single hit. A further 25 % were two-hit clusters, while the remainder
 235 were three or more hit clusters.

236 Due to trapping effects and lower overall charges for irradiated sensors, one hit clusters are
 237 more often observed than in unirradiated samples. With increasing bias voltage the number of two

⁴Fraunhofer-Institut für Zuverlässigkeit und Microintegration, Berlin

238 hit clusters rises since it becomes more likely that a neighbouring pixel is above threshold as well.
 239 This behaviour can be clearly seen in Figure 3.

sample	V_{bias} [V]	CS=1 [%]	CS=2 [%]	CS=3 [%]	Charge sharing probability [%]
MPP1	150	65	31	2	33
MPP1	200	60	36	2	37
MPP2	200	75	23	1	24
MPP3	150	71	25	1	27
MPP4	250	95	4	1	4
MPP4	350	92	6	1	7
MPP4	500	88	9	1	10
MPP4	550	87	11	1	11
MPP4	700	85	13	1	14
MPP5	500	87	11	1	12
MPP5	550	78	19	1	21

Table 2. Cluster size (CS) composition for CiS modules measured at different bias voltages during beam tests; clusters were matched to a track. Charge sharing probability is also reported.

240 **Collected charge** The collected charge was measured as a function of the bias voltage for the
 241 different sensors. In Figure 4 the sub-pixel resolved charge collection profile is shown for MPP3
 242 at V_{bias} of 150 V. The most prominent feature is the lower collected charge value on the right hand
 243 side, corresponding to the bias dot region where the pixel implant is connected to the bias grid.
 244 The same effect is evident in n-in-n devices with the same design (Section 5). In this region the
 245 collected charge is still well above the threshold.

246 Figure 5 shows lower collected charge along the edges of a pixel, due to charge sharing with the
 247 neighboring pixels. As charge sharing occurs, less charge is available for the pixel traversed by
 248 the particle, decreasing the probability to pass the electronics threshold. This effect is especially
 249 pronounced in the corners of the pixel, as charge can be shared among four pixels. However, in
 250 these regions the deposited charge is still high enough for an efficient operation of the device.

251 Figure 6 shows the most probable charge for all samples. For comparison the charge collected
 252 by unirradiated devices (MPP1 and MPP2) is included and a typical discriminator threshold of
 253 3200 e is indicated. A systematic error on the collected charge of 400 e is assumed, due to the finite
 254 charge resolution of the ToT mechanism; a 5% systematic uncertainty is taken into account, due to
 255 non-uniformity in the injection capacitances.

256 Although the irradiated samples do not show saturation of the collected charge up to 700 V,
 257 already at low bias voltages the collected charge exceeds the electronics threshold by more than a
 258 factor of two and can thus be considered safe for tracking applications.

259 **Charge sharing** In Figure 7 (top) the charge sharing probability within one pixel for MPP3 is
 260 shown. At normal track incidence increased charge collection probability is evident at the edges
 261 and corners of the pixel. The situation after irradiation is shown in Figure 7 (bottom). Here the

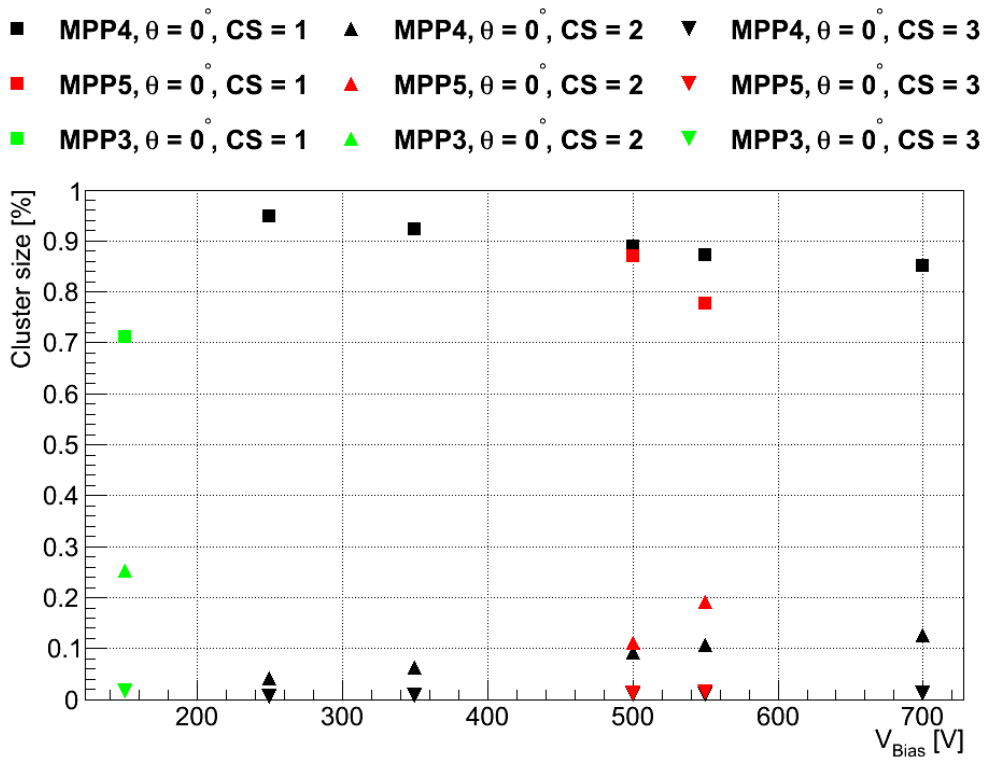


Figure 3. Relative cluster size abundance as a function of bias voltage for irradiated MPP4 and MPP5 devices. MPP3 (non-irradiated) are added for comparison. Particles were impinging at normal incidence. Errors on fractions are negligible and so not visible in the plot.

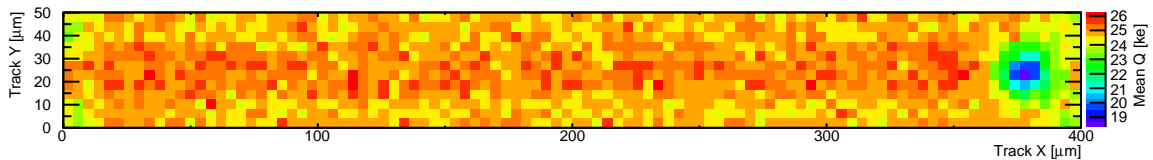


Figure 4. Charge collection within a single pixel by track position for MPP3 at V_{bias} of 150 V

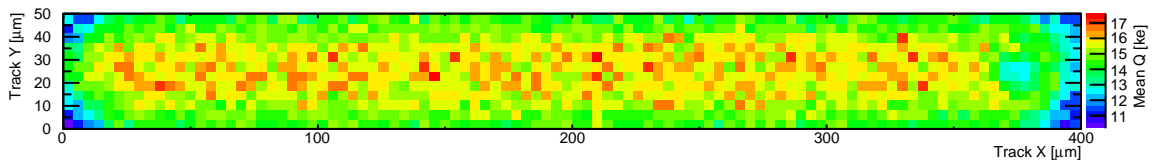


Figure 5. Charge collection within a single pixel by track position for MPP5 at $V_{\text{bias}} = 500$ V

262 charge sharing especially on the side of the punch through biasing is reduced, since there is a higher
 263 probability for the neighbouring pixel to be below threshold. This is also reflected in the average

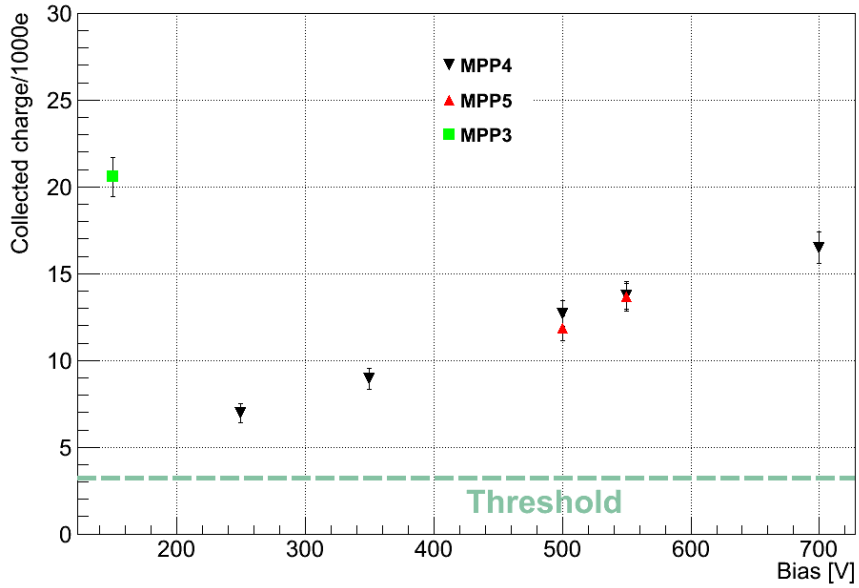


Figure 6. Charge collected in a cluster: most probable value of the charge distribution fitted to a Landau function convoluted with a gaussian as a function of the bias voltage. See text for the discussion on the assigned systematic uncertainty. The threshold value is also depicted as a dashed line.

264 charge sharing probability given in Table 2 for the n-in-p CiS detectors in all states. With increasing
 265 bias voltage an increase of the charge sharing is observed for the irradiated sensors (MPP4, MPP5)
 266 due to the increase in the collected charge.

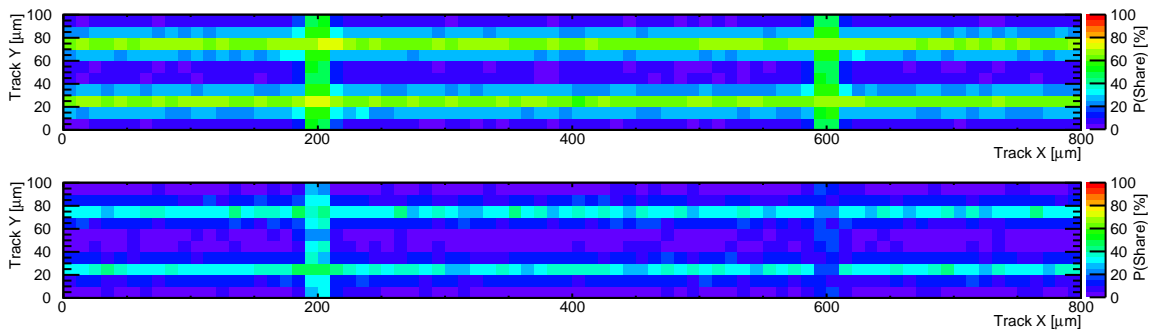


Figure 7. Charge sharing map for MPP3 detector, biased at 150 V (top) and for MPP4 detector, biased at 700 V.

267 **Residuals** Figure 8 shows the cluster position residual distribution for the irradiated module
 268 MPP5, biased at 500 V. The spatial resolution is compatible with the digital resolution, as one-

269 hit clusters are dominant. For comparison, the residual distribution for MPP3 at 150 V is shown in
 270 Figure 9. No difference is appreciable between the two samples.

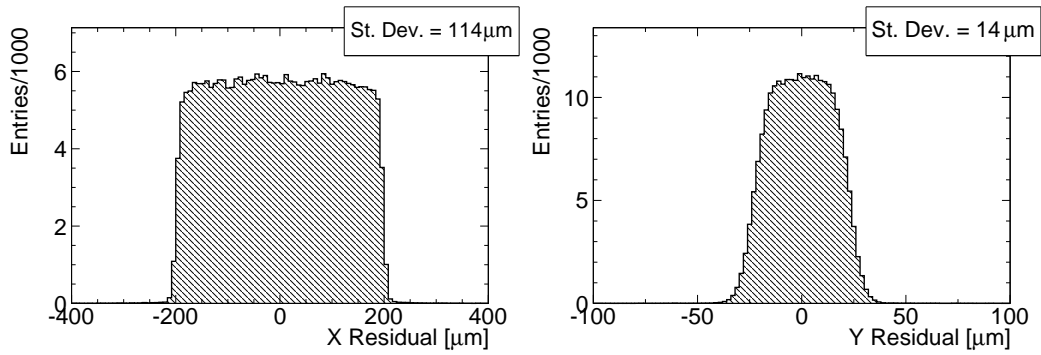


Figure 8. Residual distribution for irradiated sample MPP5 at V_{bias} of 500 V. Left: long pixel projection; right: short pixel projection.

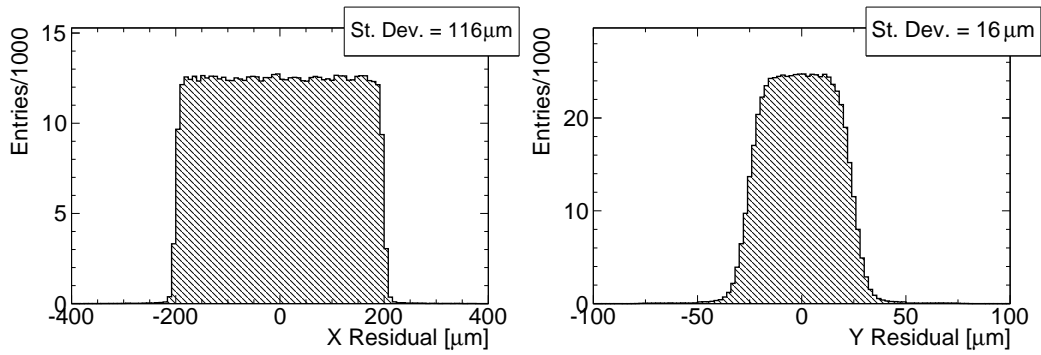


Figure 9. Residual distribution for non-irradiated MPP3 biased at 150 Volts. Left: long pixel projection; right: short pixel projection.

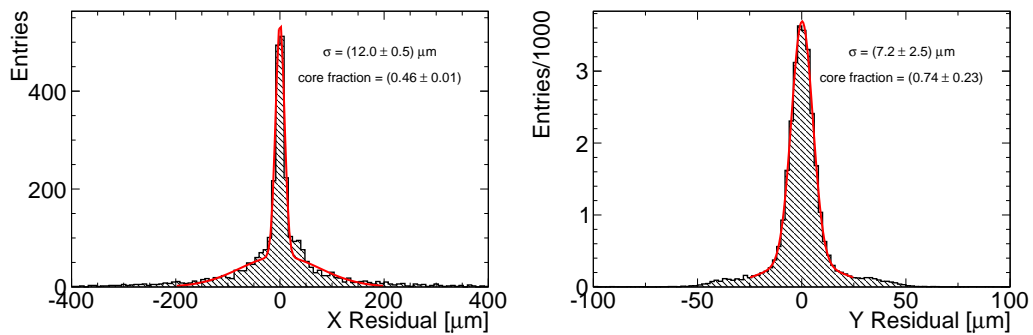


Figure 10. Residual distribution for irradiated sample MPP5 biased at V_{bias} of 500 V, for two-hit clusters. Left: long pixel projection; right: short pixel projection.

271 For the irradiated assembly MPP5 Figure 10 shows in case of two hit clusters a resolution of
 272 $(7.2 \pm 2.5) \mu\text{m}$ in the core gaussian along the short pixel direction. For comparison, Figure 11 shows
 273 the two-hit cluster residuals for MPP3 at 150 V. After irradiation there are more noise related hits,
 274 clearly visible in Figure 10. The fitted core fraction indeed decreases with respect to unirradiated
 275 sample (Figure 11). Nonetheless, the tracking capabilities of irradiated DUTs, in terms of spatial
 276 resolution, are still satisfactory.

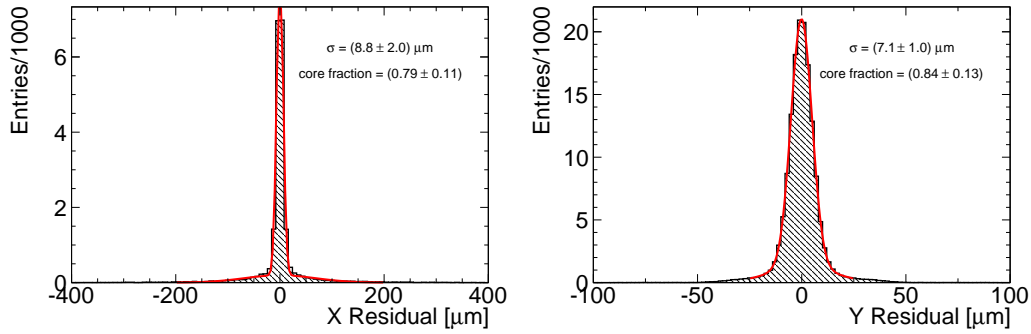


Figure 11. Residual distribution for unirradiated sample MPP3 at V_{bias} of 150 V, for two-hit clusters. Analysis restricted to clusters with 2 pixels. Left: long pixel projection; right: short pixel projection.

277 4.2 HPK sensors

278 In the following the p-type sensors produced at HPK will be introduced and their beam test results
 279 discussed.

280 4.2.1 Sensors design

281 Two modules with different sensor n-in-p layouts were subject to beam tests; one with a polysilicon
 282 bias resistor and a common p-stop isolation (KEK1), and the other with a polysilicon bias resistor
 283 and an individual p-stop isolation (KEK2). Figure 12 shows a sketch of the pixel cell design for
 284 these two samples. The sensors came from Float Zone (FZ) wafers with 100 crystal orientation;
 285 the wafer thickness was $320 \mu\text{m}$. The measured wafer resistivity was approximately $6 \text{ k}\Omega\text{cm}$.

286 A metal bias rail runs along each pixel double-column; there is no bias rail implant underneath
 287 it [22]. A parylene coating has been applied to the front side of the n-in-p pixel. The modules were
 288 tested before any irradiation and the depletion voltage was about 180 V.

289 4.2.2 Beam test results

290 The HPK samples characterization has been carried out by measuring the cluster size, collected
 291 charge, charge sharing and spatial resolution as a function of the bias voltage.

292 **Cluster Size** The KEK1 and KEK2 samples were biased at 100 V and 200 V. The two samples
 293 perform in a similar way in terms of cluster size for particles at normal track incidence. As shown
 294 in Table 3 (see also Figure 13) more than 80% of the clusters have just one hit pixel at 100 V bias
 295 voltage. As the bias voltage increases, the fraction of 2-pixel clusters also increases, as more charge

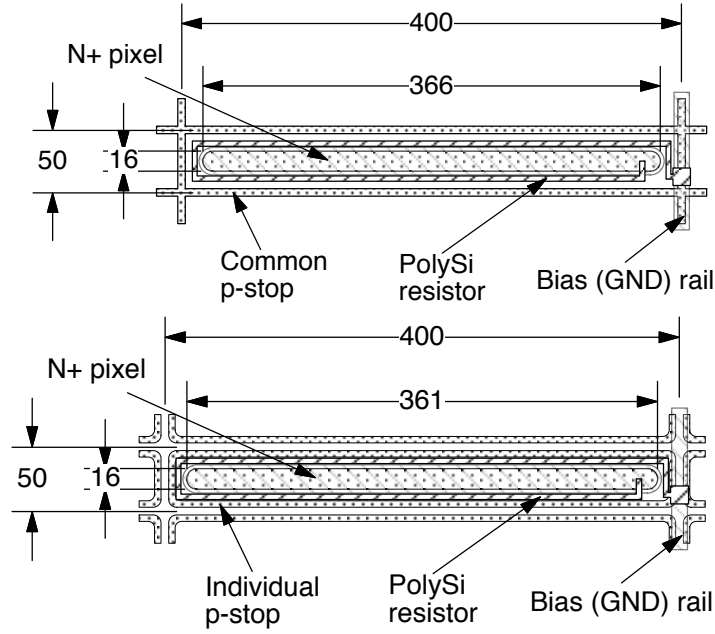


Figure 12. Pixel cell design details for KEK1 (top) and KEK2 (bottom) samples.

296 is collected. Therefore the charge fluctuations are small compared to the threshold, which reduces
 297 the probability of a pixel collecting a signal below threshold.

sample	V_{bias} [V]	CS=1 [%]	CS=2 [%]	CS=3 [%]	Charge sharing probability [%]
KEK1	100	81	16	1	18
KEK1	200	73	23	2	26
KEK2	100	83	14	1	16
KEK2	200	76	20	2	22

Table 3. Cluster composition for HPK detectors for different bias voltages; charge sharing probability is reported in the last column. Clusters were matched to a track.

298 **Collected charge** In Figure 14 the collected charge per cluster is shown as a function of bias
 299 voltage for the KEK sensors. The charge collection improves with bias voltage, but already at
 300 100 V the signal is more than 4 times the threshold. At 200 V the expected full charge is collected.

301 **Charge sharing** Figure 15 shows the charge sharing map for KEK1. At normal incidence the
 302 fraction of charge sharing is more than 25 % for a sensor biased at 200 V. Results for KEK2 show
 303 that the charge sharing is less effective (22 %): this can be related to the different layout between
 304 the two sensors. In the bottom figure the combined effect of the bias metal rail and the individual
 305 p-stop is visible. Results are summarized in Table 3.

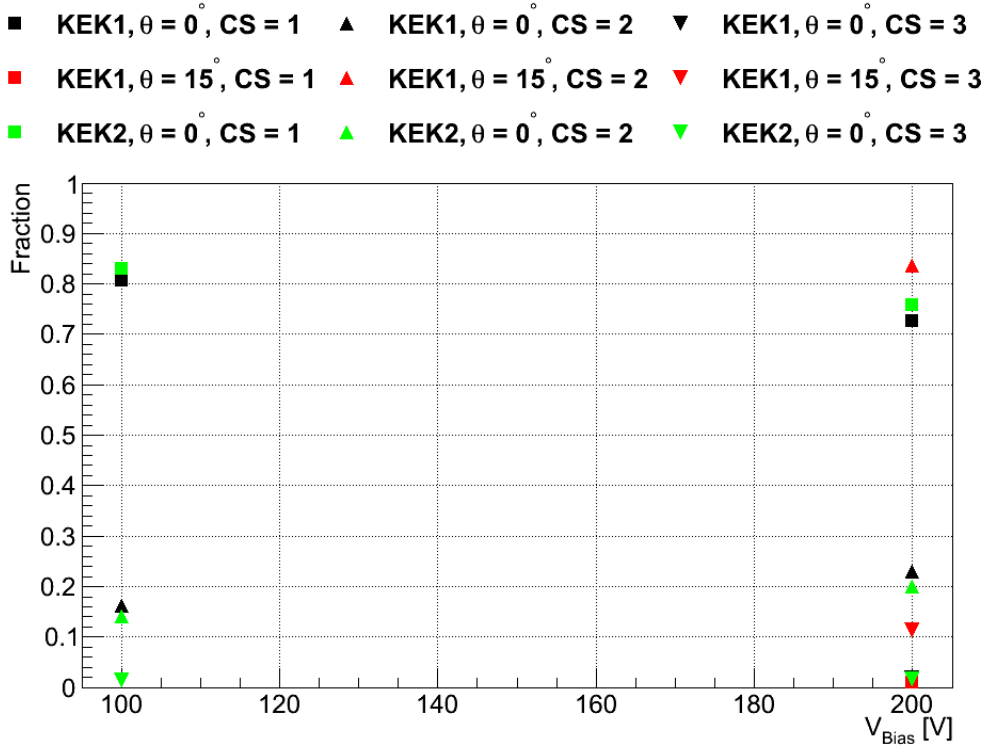


Figure 13. Fraction of cluster sizes as function of the bias voltage for HPK samples; particles were impinging at different angles too.

306 **Residuals** Figure 16 shows the residual distribution for all clusters at normal track incidence.
 307 The spatial resolution is about $16 \mu\text{m}$ along the short pixel direction, which is comparable with the
 308 digital resolution of $\text{pitch}/\sqrt{12}$; the same is true for the long pixel direction (RMS about $116 \mu\text{m}$).
 309 No difference is noticeable between KEK1 and KEK2 sensors.

310 Figure 17 shows the residual distribution for two-hit clusters. For these, the spatial resolution
 311 is found to be around $7 \mu\text{m}$ in the short pixel direction and around $9 \mu\text{m}$ for the long one (see
 312 also Table 4). The spatial resolution when the cluster contains two hits is larger than the telescope
 313 pointing-resolution and gives an estimate of the charge sharing region between neighbouring pixels.

314 5. Radiation hardness of n-in-n sensors

315 The n-in-n sensor technology used in the current ATLAS Pixel detector have been tested to fluences
 316 up to $1.1 \times 10^{15} \text{ n}_{\text{eq}}/\text{cm}^2$ [11]. To evaluate the usability of n-type bulk material for IBL and future
 317 detector upgrades, sensors have been irradiated with fluences as high as $2 \times 10^{16} \text{ n}_{\text{eq}}/\text{cm}^2$ using
 318 both reactor neutrons (Jožef-Stefan Institute, Ljubljana) [18] and protons of 25 MeV (Karlsruhe
 319 Institute of Technology - KIT) [19] or 24 GeV (CERN) [12].

320 Most of the sensors follow the ATLAS Pixel detector sensor design with 16 guard rings and
 321 a thickness of $250 \mu\text{m}$. DO6 is a special sensor with only 11 guard rings overlapping the pixel

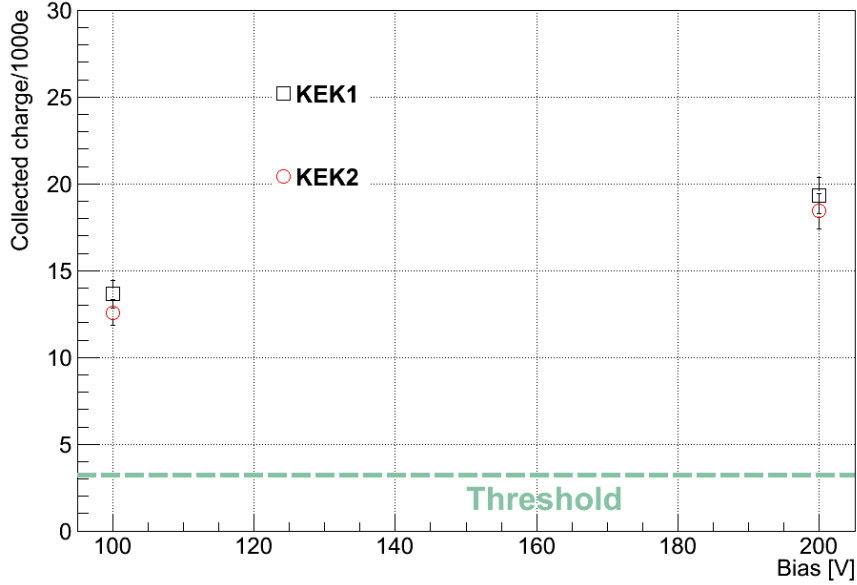


Figure 14. Collected charge as a function of the bias voltage for HPK samples; particles were impinging at different angles too. A threshold of 3200 e is indicated.

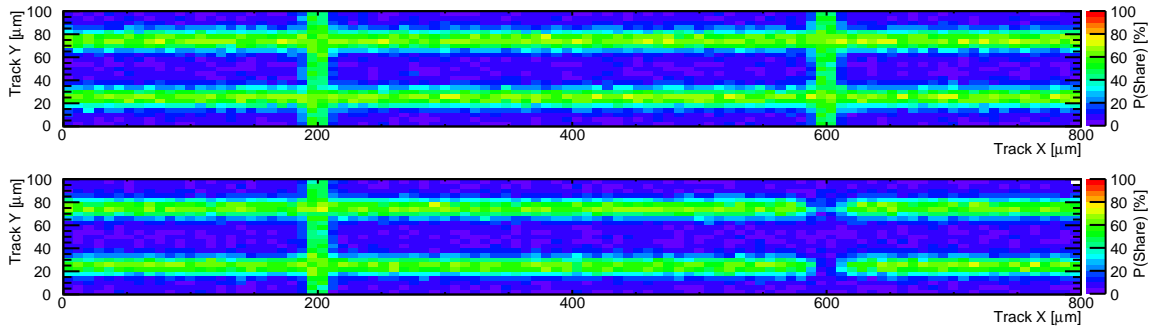


Figure 15. Charge sharing map for KEK1 (top) and KEK2 (bottom) at V_{bias} of 200 V.

322 region, designed to study possibilities to reduce the inactive area at the edge of the sensor (see
 323 section 6) and produced on 285 μm thick bulk material. The n-type sensors were produced at CiS,
 324 from Diffusion Oxygenized Float Zone (DOFZ), 111 oriented wafers; the wafer resistivity was in
 325 the range between 2 and 5 $\text{k}\Omega$. The depletion voltage was in the range between 30 and 70 V for
 326 200 μm thick sensors, between 40 and 100 V for 250 μm thick sensors and between 50 and 140 V
 327 for 285 μm thick sensors.

328 A total of 5 irradiated n-in-n pixel sensors were tested. Table 5 summarizes the fluences to
 329 which the sensors were irradiated. See also [16].

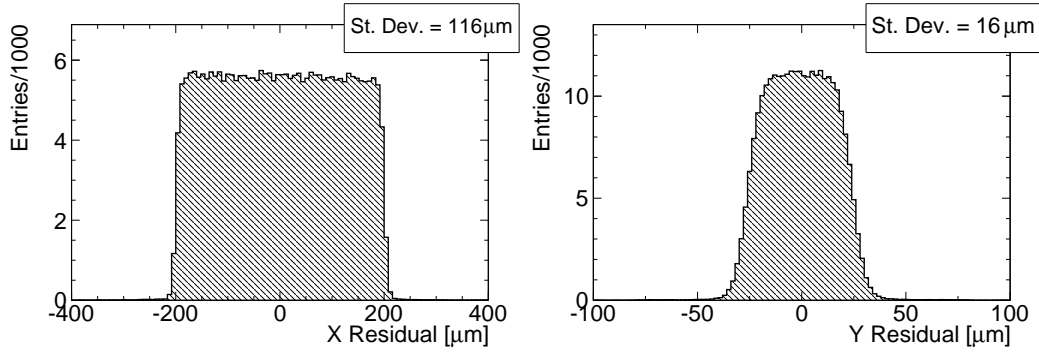


Figure 16. Cluster position residual distribution for non-irradiated sample KEK1 at V_{bias} of 200 V at normal incidence. Left: long pixel projection; right: short pixel projection.

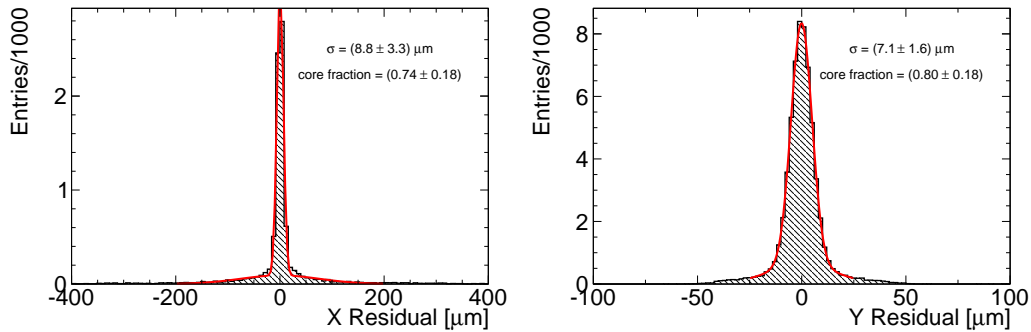


Figure 17. Residual distribution for non-irradiated KEK1 biased at 200 Volts clusters with 2 pixels. Left: long pixel projection; right: short pixel projection.

Sample	V_{bias} [V]	pitch (μm)	RMS (μm)	core σ (μm)	core fraction [%]
KEK1	100	400	116.00 ± 0.14	9.00 ± 0.13	68
KEK2	100	400	115.00 ± 0.14	9.40 ± 0.20	53
KEK1	200	400	116.10 ± 0.20	9.0 ± 3	74
KEK2	200	400	115.00 ± 0.15	9.31 ± 0.18	60
KEK1	100	50	16.000 ± 0.020	7.14 ± 0.06	78
KEK2	100	50	15.800 ± 0.020	6.88 ± 0.05	78
KEK1	200	50	15.90 ± 0.05	7.1 ± 1.6	80
KEK2	200	50	16.000 ± 0.021	6.81 ± 0.05	79

Table 4. Summary of residual results for KEK1 and KEK2 samples. Core σ and fraction are evaluated for 2-pixels clusters only.

330 5.1 Results

331 **Charge collection** One of the main effects of irradiation is the increased trapping, which leads
 332 to a reduced signal amplitude. As the trapping probability depends on the charge carrier velocity,

name	thickness (μm)	fluence ($10^{15} \text{ n}_{\text{eq}}/\text{cm}^2$)	irradiation type
DO6	285	0	–
DO7	250	1	protons (KIT)
DO8	250	1	reactor neutrons
DO9	250	5	reactor neutrons
DO10	250	20	reactor neutrons

Table 5. Summary of irradiated n-in-n samples in the testbeams. KIT stands for 25 MeV energy proton irradiation.

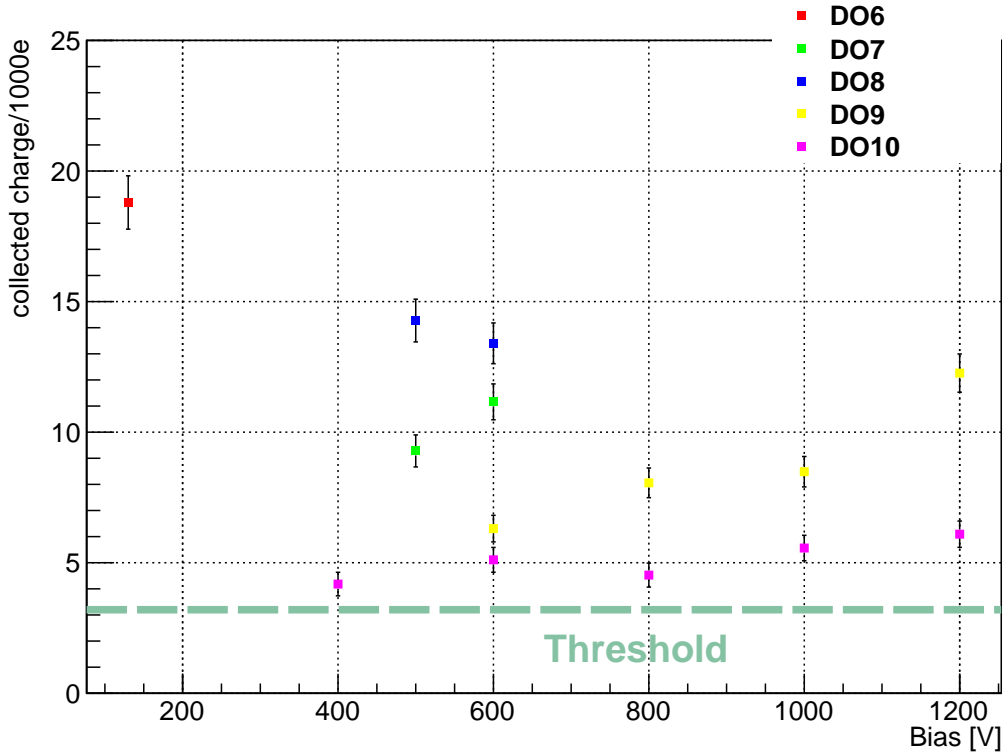


Figure 18. Collected charge as a function of bias voltage for n-in-n samples irradiated to different fluences (see details in the text). A threshold of 3200 e is indicated.

333 the collected charge was measured as a function of the bias voltage. Figure 18 shows the results
334 for all irradiated n-in-n samples in the two beam test periods; see also Table 5. A systematic
335 error on the collected charge of 400 e is assumed, due to the finite charge resolution of the ToT
336 mechanism; a 5% systematic uncertainty is also taken into account, due to non-uniformity in the
337 injection capacitances.

338 After $5 \times 10^{15} \text{ n}_{\text{eq}}/\text{cm}^2$, the collected charge still exceeds 10 ke at a bias voltage of 1000 V. Even if
339 the collected charge is shared equally between two neighboring pixels, this charge is sufficient to
340 detect the hit with FE-I3.

341 Figure 19 top, shows that charge is predominantly lost in the region of the punch-through bias
 342 grid system.

343 At very high fluences ($2 \times 10^{16} \text{ n}_{\text{eq}}/\text{cm}^2$, DO10 sample) it is no longer possible to say which
 region is less efficient than the others, using the charge collection method (Figure 19, bottom).

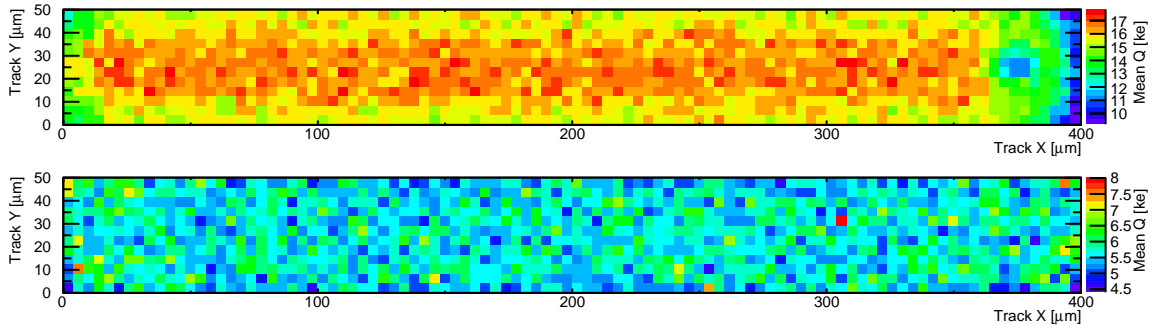


Figure 19. Charge collection within a pixel. Top: DO9 at $V_{\text{bias}}=1200 \text{ V}$. Bottom: DO10 at $V_{\text{bias}}=1000 \text{ V}$.

344

345 **Charge sharing** Figure 20 shows the charge sharing probability for DO9 at a bias voltage of
 346 1200 V. Reduced charge sharing probability is visible in the region of the bias dot and the bias grid
 347 network.⁵ Less charge is deposited here, so there is a higher probability for the second pixel in a
 348 two-pixel cluster to be below threshold. As only the bias trace makes the difference between both
 349 pixel sides, it might cause the lower charge sharing probability. Furthermore, one can see that the
 350 region of the bias dot is not affected.

351 While for DO9 a clear increase in charge sharing probability towards the edges of the pixel is
 352 visible, at higher fluence the collected charge becomes too small for any significant charge sharing
 353 to be observable. This can also be seen in the fractions of clusters with one, two, and more pixels.
 Figure 21 shows the fractions of one-pixel, two-pixel, and larger clusters as a function of the bias

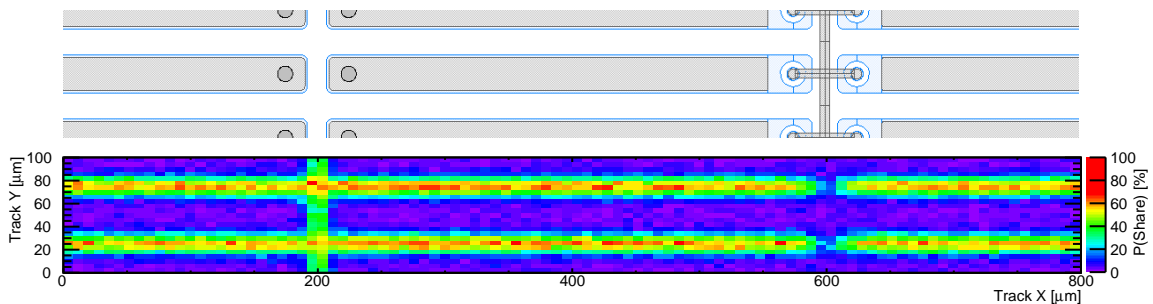


Figure 20. Top: Design of the sample of the region shown in the plot below. Bottom: Charge sharing probability for DO9 at $V_{\text{bias}}=1200 \text{ V}$. Note the reduced charge sharing in the bias grid region on the right-hand side of the central pixel.

354

⁵The bias grid network is an aluminum trace arranged on top of the intermediate pixel region connecting all bias dots.

355 voltage. It is evident, that with increasing bias voltage the cluster size increases, due to the reduced
 356 trapping. At a given voltage the fraction of 1-pixel clusters increases with fluence, as more charge
 357 is lost due to trapping.

358 For samples irradiated up to $5 \times 10^{15} \text{ n}_{\text{eq}}/\text{cm}^2$ the cluster size increases slightly with bias voltage,
 359 while at $2 \times 10^{16} \text{ n}_{\text{eq}}/\text{cm}^2$ the fraction of clusters with two or more hit pixels is very small and stays
 nearly constant over the accessible voltage range.

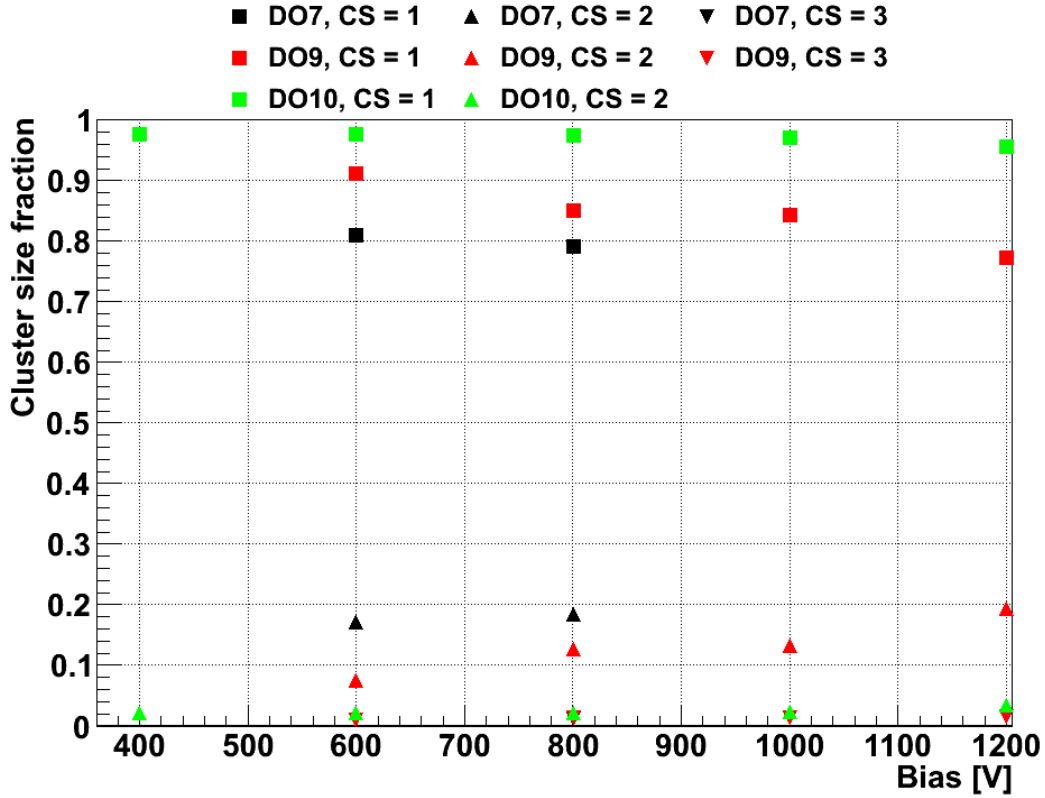


Figure 21. Fractions of 1-, 2-, and 3-hit clusters as function of bias voltage for irradiated n-in-n samples; see text for details. Error bars are too small to be visible.

360

361 Plotting the residual distribution for two-pixel clusters only allows the width of the charge
 362 sharing region between pixels to be determined. Figure 22 shows the distributions for DO9 ($5 \times$
 363 $10^{15} \text{ n}_{\text{eq}}/\text{cm}^2$) and DO10 ($2 \times 10^{16} \text{ n}_{\text{eq}}/\text{cm}^2$). After correcting for the telescope resolution, the
 364 widths of the charge sharing regions are $7.1 \mu\text{m}$ and $7.7 \mu\text{m}$. These values correspond very well
 365 with the width found for an unirradiated sample of $6.4 \mu\text{m}$. This indicates that the lateral diffusion
 366 of the charge cloud does not change significantly with irradiation.

367 **Residuals** Figure 23 shows the residual distributions in the $50 \mu\text{m}$ pixel direction for the unirra-
 368 diated sample (DO6) and the sample irradiated to $2 \times 10^{16} \text{ n}_{\text{eq}}/\text{cm}^2$, respectively. The widths of the
 369 distributions are $16 \mu\text{m}$ and $15.4 \mu\text{m}$, comparable with the expected digital resolution of $14.4 \mu\text{m}$.
 370 Thus, no influence of radiation damage on the spatial resolution can be observed.

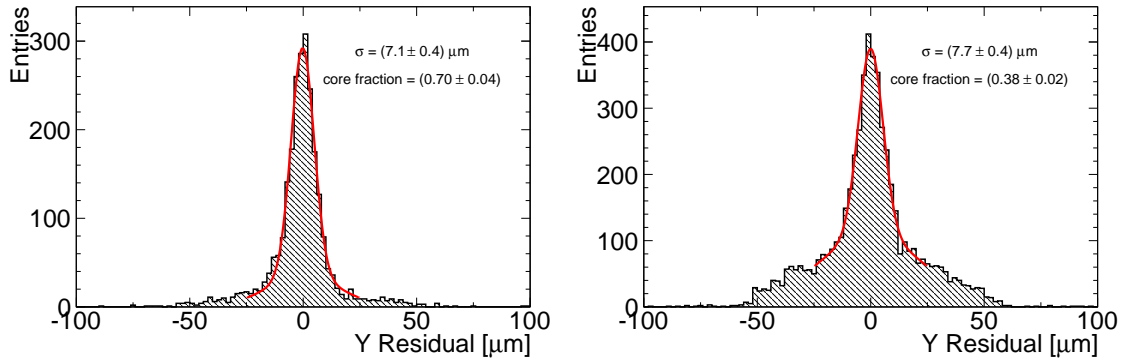


Figure 22. Residual distributions for 2-pixel clusters only. Shown are distributions samples irradiated to $5 \times 10^{15} \text{ n}_{\text{eq}}/\text{cm}^2$ (left: DO9, bias voltage 1000 V) and $2 \times 10^{16} \text{ n}_{\text{eq}}/\text{cm}^2$ (right, DO10, bias voltage 1200 V), respectively.

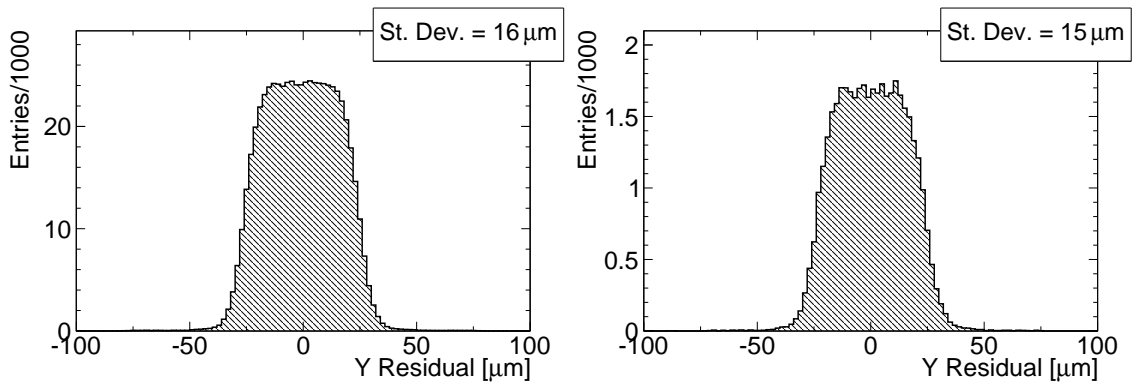


Figure 23. Residual distributions in the short pixel direction for an unirradiated sample (DO6, left) and a sample irradiated to $2 \times 10^{16} \text{ n}_{\text{eq}}/\text{cm}^2$ operated at a bias voltage of 1000 V (DO10, right). No deterioration of the spatial distribution with irradiation is visible.

371 6. Slim Edge

372 For slim edge studies the outermost pixels of a sample are of special interest. Therefore, the samples
 373 were mounted such that the edge of the sensor was well within the trigger acceptance window.
 374 Special analysis classes were written to investigate the characteristics of the edge pixels. The basic
 375 principle is the same as for the charge collection analysis but instead of overlaying all pixels onto
 376 one single pixel, only pixels at the sensor edge are used and the special geometry is conserved in
 377 the overlay process.

378 For the IBL sensors the width of the inactive region at the edge of each sensor tile has to be re-
 379 duced significantly with respect to the approximately 1 mm wide region on each side of the current
 380 ATLAS Pixel detector sensors. One approach is to shift the guard-rings on the p^+ -side inwards.
 381 Two specially designed DUTs were tested to study the impact of an overlap between the active
 382 pixel region with the guard ring region, where the electric field in the sensor is inhomogeneous.

383 In the DO6 sample, the overlap between active pixel region and guard ring region is $210\ \mu\text{m}$, with
 384 the number of guard rings reduced to 11. In the DO3 sample groups of 10 pixels are shifted towards
 385 the edge of the sensor in steps of $25\ \mu\text{m}$, increasing the area in which the pixels overlap with the
 386 guard-rings (see Figure 24).

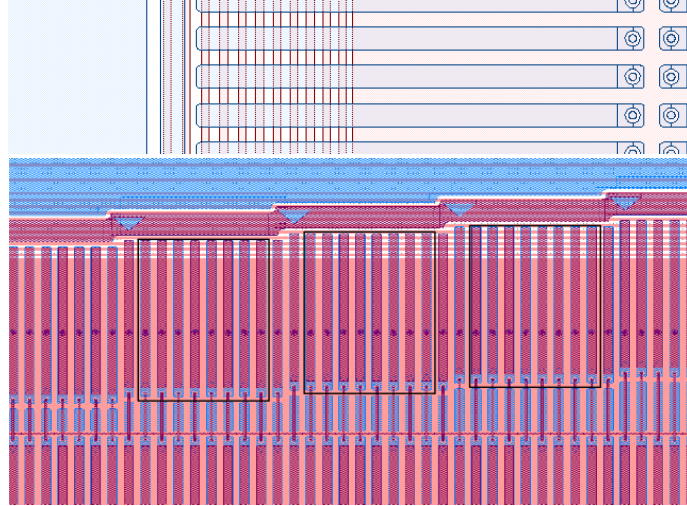


Figure 24. Test structures for slim edge studies. Top: DO6, the active pixel region overlaps the guard rings by $210\ \mu\text{m}$. Bottom: DO3, groups of 10 pixels shifted towards the edge of the sensor in steps of $25\ \mu\text{m}$.

387 The test structures were mounted such that the edge of the sensor was well in the center of the
 388 trigger window, allowing to study charge collection in the shifted pixels in some detail. Figure 25
 389 shows the collected charge in the overlap region of DO6. With increasing distance from the bias
 390 voltage pad the collected charge decreases, due to the inhomogeneously formed depletion zone. It
 391 is evident that the collected charge is sufficient to ensure good hit efficiency up to about $200\ \mu\text{m}$
 392 from the edge of the bias voltage pad.

393

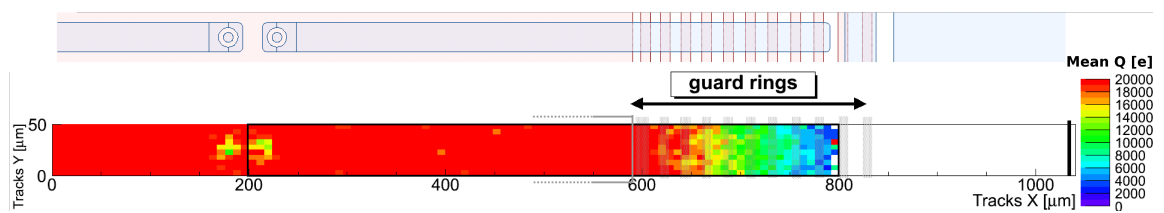


Figure 25. Charge collection in the pixels shifted underneath the guard rings.

394 Figure 26 shows the collected charge in the overlap region for the DO3 sample. Data from
 395 pixels with the same shift with respect to the edge of the bias voltage pad are plotted into one pixel.
 396 The drop in collected charge systematically occurs at the same distance from the bias voltage pad,
 397 regardless of the shift of the pixel. This indicates, that the loss of collected charge is indeed due to
 398 the depletion zone which is expected to be inhomogeneous along the x-axis (orthogonal to the bias

399 voltage pad) but homogeneous along the y-axis (parallel to the bias voltage pad). Further studies
 400 of this kind can be found in [32].

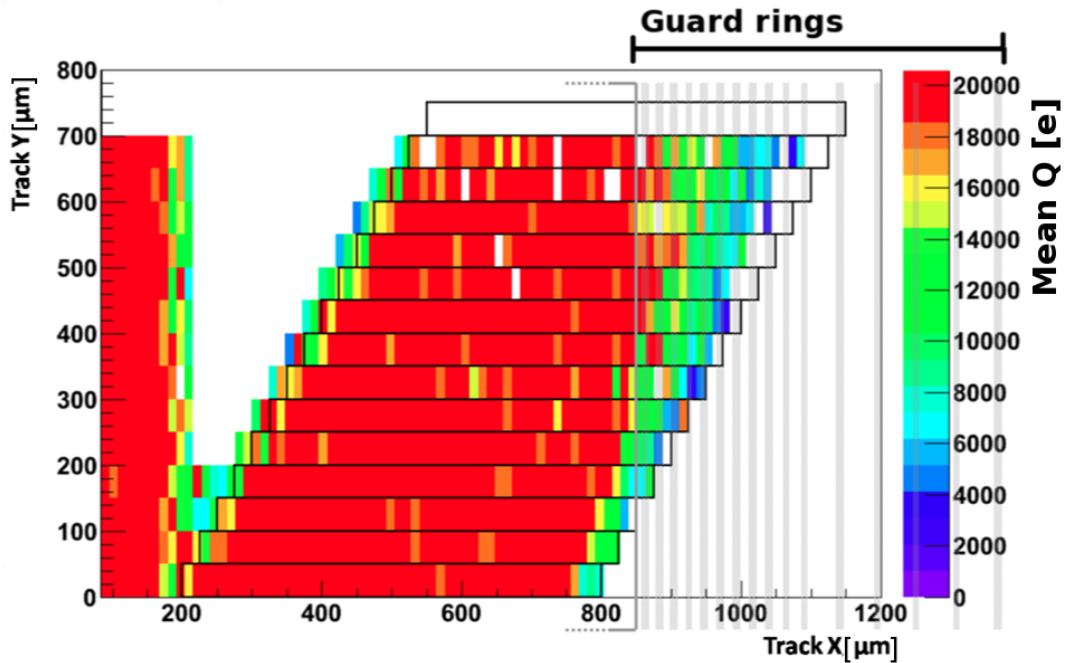


Figure 26. Charge collection in the pixels shifted underneath the guard rings.

401 7. Conclusion

402 Planar silicon sensors have been tested in high energy pion beams at the CERN SPS North Area in
 403 2010 by the ATLAS Planar Pixel Sensors (PPS) collaboration.

404 The goals of the measurement program were threefold: to demonstrate the suitability of p-bulk
 405 sensors for tracking purposes, to prove the radiation hardness of n-bulk sensors and to realize pixel
 406 sensors with reduced inactive edge area.

407 Pixelated p-bulk sensors produced by several vendors were tested to evaluate their performance
 408 before and after irradiation. In terms of the collected charge, charge sharing, and spatial resolution
 409 the performance of the p-bulk sensors was very good and comparable to that of n-bulk sensors.
 410 The issue of the high potential on the pixelated side of the sensor was tested and operation of the
 411 sensors was proven to be very stable.

412 The radiation hardness of n-bulk sensors was tested up to unprecedented fluences, with a
 413 maximum of $20 \times 10^{15} \text{ n}_{\text{eq}}/\text{cm}^2$. At a bias voltage of 1.2 kV the collected charge was about 6 ke,

414 which is sufficient to guarantee reasonable hit efficiency. Despite the rather small collected charge
415 and the reduced charge sharing between pixels, no significant deterioration of the spatial resolution
416 was observed.

417 In order to reduce the inactive area at the edge of n-bulk sensors, several modified sensor
418 layouts were tested. The influence of a reduction of the number of guard rings and an increasing
419 overlap between the active pixel region and the guard ring region on the backside of the sensor
420 were studied. It was found that the charge collection efficiency reduces with increasing distance
421 from the edge of the bias voltage pad due to the inhomogeneously formed depletion zone in the
422 sensor. However, the collected charge is sufficient for reliable particle detection up to a distance
423 of about $200\ \mu\text{m}$ from the bias voltage pad. This was very encouraging for the planar ATLAS IBL
424 candidate design, which was finally designed employing the methods evaluated by the beam test
425 measurements described in this paper.

426 Acknowledgements

427 The authors would like to express their gratitude to V. Cindro, G. Kramberger and I. Mandić for
428 their valuable support with irradiations at the TRIGA reactor of the Jožef Stefan Institute, Ljubljana,
429 to A. Dierlamm for his help at the Irradiation Center, Karlsruhe, and to M. Glaser for his help
430 at the CERN PS irradiation facility.

431 The work has been partially performed in the framework of the CERN RD50 Collaboration.
432 This work is supported by the Commission of the European Communities under the 6th Framework
433 Programme “Structuring the European Research Area”, contract number RII3-026126.

434 We gratefully acknowledge the financial support of the German Federal Ministry of Science
435 and Education (BMBF) within their excellence program, in particular as part of the collaborative
436 research center “FSP 101-ATLAS, Physics on the TeV-scale at the Large Hadron Collider”.

437 We acknowledge the support of the Initiative and Networking Fund of the Helmholtz Association,
438 contract HA-101 (“Physics at the Terascale”).

439 References

- 440 [1] *ATLAS Pixel Detector Electronics and Sensors*,
441 The ATLAS collaboration, JINST 3 P07007, 2008
- 442 [2] *ATLAS Insertable B-Layer Technical Design Report*,
443 ATLAS TDR 19, CERN/LHCC 2010-013,
444 <http://cdsweb.cern.ch/record/1291633/files/ATLAS-TDR-019.pdf>
- 445 [3] *LHC near and medium term prospect*,
446 M. Lamont, <http://dx.doi.org/10.3204/DESY-PROC-2010-01/8>
- 447 [4] *Stragglings in thin silicon detectors*,
448 H. Bichsel, Rev. Mod. Phys. **60** 663 (1988)
- 449 [5] *Diamond pixel modules*,
450 D. Asner *et al.*, Nucl. Instr. Meth. **A636**, 125 - 129 (2011).
- 451 [6] *3D silicon pixel sensors: Recent test beam results*,
452 P. Hansson *et al.*, Nucl. Instr. Meth. **A628**, 216 - 220 (2011).
- 453 [7] ATLAS Upgrade Planar Pixel Sensor R&D Project,
454 see also <https://edms.cern.ch/document/966140>
- 455 [8] *Results from the EUDET telescope with high resolution planes*,
456 A. Bulgheroni *et al.*, Nucl. Instr. Meth. **A623**, 399-401 (2010).
- 457 [9] *The FEI3 readout chip for the ATLAS pixel detector*,
458 I. Perić *et al.*, Nucl. Instr. and Meth. **A565** 178 - 187 (2006).
- 459 [10] TurboDAQ
- 460 [11] *Test beam performance of the ATLAS Pixel Detector modules*,
461 A. Andreazza on behalf of the ATLAS Pixel Collaboration, Nucl. Instr. Meth. **A565**, 23 - 29 (2006).
- 462 [12] *New irradiation zones at the CERN-PS*,
463 M. Glaser *et al.*, Nucl. Instr. Meth. **A426**, 72 - 77 (1999).

- 464 [13] *Spatial resolution of silicon microstrip detectors*,
465 R. Turchetta Nucl. Instr. Meth. **A335**, 44 - 58 (1993).
- 466 [14] *Highly segmented thin microstrip detector with data-driven fast readout*,
467 M. Bomben *et al.*, Nucl. Instr. Meth. **A623** 159-161 (2010).
- 468 [15] *Design studies on sensors for the ATLAS Pixel Detector*,
469 F. Hüggling, Nucl. Instr. Meth. **A477** 143-149 (2002).
- 470 [16] *Radiation hardness studies of n^+ -in- n planar pixel sensors for the ATLAS upgrades*,
471 S. Altenheiner *et al.*, Nucl. Instr. Meth. **A658**, 25 - 29 (2011).
- 472 [17] *Development and operation of a testbeam setup for qualification studies of ATLAS pixel sensors*,
473 G. Troska, Ph. D. Thesis, TU Dortmund, 2012
- 474 [18] *Analysis of neutron flux distribution for the validation of computational methods for the optimization
475 of research reactor utilization*,
476 L. Snoj *et al.*, Appl. Rad. and Iso. **69** (2011) 136
- 477 [19] Irradiation Center of Karlsruhe Institute of Technology (KIT)
- 478 [20] *Characterization and performance of silicon n-in-p pixel detectors for the ATLAS upgrades*,
479 P. Weigell *et al.*, Nucl. Instr. and Meth. **A658** 36 - 40 (2011).
- 480 [21] *Measurements of spatial resolution of ATLAS pixel detectors*,
481 T. Lari *et al.*, Nucl. Instr. and Meth. **A465** 112 - 114 (2001).
- 482 [22] *Development of n-in-p silicon planar pixel sensors and flip-chip modules for very high radiation
483 environments*,
484 Y. Unno *et al.*, Nucl. Instr. and Meth. A **650** (2011), p. 129
- 485 [23] *Test Beam Measurements with the EUDET Pixel Telescope*,
486 J. Behr, <http://www.eudet.org>, EUDET-Report-2010-01
- 487 [24] *A Trigger/Timing Logic Unit for ILC Test-beams*,
488 D. Cussans, Contribution to “TWEPP-07 Topical Workshop on Electronics for Particle Physics”,
489 3-7 September 2007, Prague (Czech Republic)
- 490 [25] *A ten thousand frames per second readout MAPS for the EUDET beam telescope*,
491 C. Hu-Guo, CERN-2009-008
- 492 [26] *Jets at High Q^2 at HERA and Test Beam Measurements with EUDET Pixel Telescope*,
493 J. Behr, Dissertation & Ph. D. thesis (2010) - ZEUS, Universität Hamburg, Chapter 16
- 494 [27] *MILLPEDE*,
495 V. Blobel, <http://www.desy.de/~blobel>
- 496 [28] *Full simulation of a testbeam experiment including modeling of the Bonn Atlas Telescope and Atlas
497 3D pixel silicon sensors*,
498 K. N. Sjøbæk, Thesis presented for the Master of Science degree in Experimental Particle Physics,
499 Department of Physics, University of Oslo, Appendix C
- 500 [29] *The Deterministic Annealing Filter*,
501 S. Fleischmann, CERN-THESIS-2007-011, pp.19 - 23
- 502 [30] *Notes on the fluence normalisation based on the NIEL scaling hypothesis*,
503 The ROSE Collaboration, Technical Note ROSE/TN/2000-02, CERN

504 [31] <http://root.cern.ch>

505 [32] *Planar slim-edge pixel sensors for the ATLAS upgrades,*
506 T. Wittig *et al*, 2012_JINST_7_C02051